Error Probability Performance of Chirp Modulation in Uncoded and Coded LoRa Systems

Giuseppe Baruffa[a], Luca Rugini[a,b], Lorenzo Germani[a], and Fabrizio Frescura[a]

[a]Dept. of Engineering, University of Perugia, Perugia, Italy
[b]CNIT Research Unit, University of Perugia, Perugia, Italy

Abstract

This paper focuses on the error probability performance of LoRa, a long-range low-power wireless communication technology suited for the Internet of Things (IoT). We propose accurate approximations for the bit error probability of the uncoded LoRa chirp modulation in additive white Gaussian noise (AWGN) channel. Our approach, which is based on a smart modification of a union bound on the error probability, is applied to both coherent and noncoherent detection. Simulation results show that the proposed theoretical bit error rate (BER) expressions are more accurate than the existing BER approximations that use similar complexity. We show that the proposed BER expressions are valid for both orthogonal and quasi-orthogonal LoRa, and are easier to compute than the exact BER for orthogonal signaling. Moreover, we extend the theoretical performance analysis to coded LoRa systems and we propose analytical BER expressions for Hamming-coded LoRa signals with hard-decision decoding. In addition, we analyze by simulation the error probability of coded LoRa systems with soft-decision decoding in multipath channels. The obtained results (both theoretical and simulated) quantify the performance gains of channel coding with respect to uncoded transmissions, in both AWGN and multipath channels, for coded LoRa systems that use the same bandwidth (with lower bit rate) of the uncoded LoRa system.

Keywords:
Chirp modulation, Hamming codes, Log-likelihood ratio, LoRa, Probability of error

1. Introduction

LoRa is a proprietary wireless communication standard, promoted by the LoRa Alliance, used for low-power wide-area networks (LPWAN) [1, 2]. Together with other types of modulation schemes [3, 4] and sensor networks for the Internet of Things (IoT) [5], LoRa is becoming popular for IoT applications with long range communications, low power operation, and occasional channel access [6]. Typical LoRa applications presented in the literature encompass, among others, human health and wellness monitoring [7], livestock farming [8, 9], industrial environment logistics [10], forestry sensing and monitoring [11].

The LoRa physical layer, patented by Semtech Corporation [12, 13], is also known as *chirp spread spectrum (CSS)* [12] or as *frequency shift chirp modulation (FSCM)* [14], and has been investigated also in [15, 16, 17]. Chirp waveforms are sinusoids with an instantaneous frequency that linearly varies with time [12]. If the frequency change rate is positive, the LoRa chirp waveform is called an *upchirp*, while a negative frequency change rate produces a *downchirp*. The bandwidth B of LoRa signals can vary from 7.8 kHz to 500 kHz, but typical values are 125 kHz, 250 kHz, and 500 kHz [2]. The frequency band is below 1 GHz and depends on the frequency allocation allowed by international and national regulation entities; for instance, in Europe, the center frequency is 868 MHz. In LoRa, for typical bandwidth values, the symbol duration is between 0.128 ms and 32.768 ms.

LoRa data transmission is performed by encoding the information contained on the bits into the initial frequency offset of the waveforms, which is basically like an upchirp or a downchirp. By cyclically wrapping the instantaneous frequency within a specific frequency range, the bandwidth B is not exceeded [14, 17, 18]. An important parameter of the LoRa modulation is the spreading factor (SF), which is defined as the number of bits S carried by the chirp waveforms. Therefore, in LoRa, there are $S = \log_2 M$ bits per symbol, where $M = 2^S$ is the number of possible chirp waveforms in the symbol interval [2, 13]. Note that this SF definition in LoRa is different from the definition commonly used in spread spectrum systems, which usually defines the SF as the bandwidth expansion factor M [19]. In LoRa, the number of bits per symbol S can range from 6 to 12, with typical values from 7 to 12 [12, 13].

In the literature, different LoRa signal models have been proposed, with continuous-time (analog) waveforms or with discrete-time (digital) chirps, in [14, 15, 17, 18, 20]. In [14, 17, 20], a discrete-time baseband (BB) signal model is proposed, using orthogonal chirp waveforms and noncoherent detection. Vangelista, in [14], demonstrated the orthogonality of the discrete-time chirp waveforms. In [18], an analog signal model is proposed, with quasi-orthogonal chirp waveforms with coherent detection. The study in [15] demonstrates that the discrete-time orthogonal LoRa waveforms are obtained from sampling the analog LoRa chirp waveforms, which are not exactly orthogonal but quasi-orthogonal. We omit a detailed discussion about the spectral properties of analog and

discrete-time chirps, which can be found in [15]: indeed, the error probability performance does not depend directly on the spectral properties of the M waveforms, but only depends on the correlation properties of the M waveforms.

The bit error rate (BER) performance of uncoded LoRa systems have been studied by different researchers. A simulation comparison of the LoRa modulation (referred to as FSCM) with frequency-shift keying (FSK) for noncoherent detection in additive white Gaussian noise (AWGN) and multipath channels is presented in [14]. Since the exact probability of error is cumbersome to compute, [20] proposed approximated BER expressions for noncoherent detection of orthogonal LoRa signals in AWGN and Rayleigh channels. Error probability approximations and bounds have been proposed also for FSK [4, 21], for both orthogonal and nonorthogonal versions used for IoT, in AWGN and Rayleigh fading, assuming a lower signal space dimension than necessary for LoRa signals. In AWGN, a Gaussian approximation for the BER of noncoherently detected LoRa signals has been proposed in [17], which compared the LoRa performance with differential binary phase-shift keying (DBPSK) employed by SigFox. In [18], assuming quasi-orthogonal CSS, the BER is obtained by a simulation-fitting-based approach (for coherent detection in AWGN) and compared with binary phase-shift keying (BPSK) and FSK.

Theoretically, the BER for orthogonal waveforms in AWGN channels has a closed-form expression [22], but unfortunately the exact BER requires either a numerical integration (for coherent detection) or the computation of large binomial coefficients (for noncoherent detection). This makes the computation of the exact BER quite cumbersome. In addition, for nonorthogonal waveforms, a closed-form expression of the exact BER is unknown. As a consequence, [18] and [20] proposed simple BER approximations based on algebraic formulas that involve the Gaussian Q-function. On the other hand, the study of [23] aims at preserving accuracy, but requires the computation of Marcum Q-functions and of the threshold parameters inside these functions. The study of [24] starts from the simple approximation of [20] and extends the analysis to include the effect of interfering users.

In this paper, we propose improved BER approximations that use the Gaussian Q-function and algebraic formulas, for both coherent and noncoherent detection of uncoded LoRa waveforms. The proposed improved BER approximations are obtained by modeling the BER expression as a scaled version of the union bound (UB), using a scaling factor that depends on the signal-to-noise ratio (SNR) and on the number of waveforms. Simulation results and high-complexity exact BER expressions demonstrate the improved accuracy of the proposed BER approximations, which are also valid for every orthogonal signaling scheme. Our comparison also shows that, due to the large number of LoRa waveforms, the BER performance of the quasi-orthogonal LoRa waveforms is indistinguishable from the BER performance of the orthogonal LoRa waveforms, for both coherent and noncoherent detection cases. As a side result, using the LoRa model of [15], in this paper we also derive the discrete Fourier transform (DFT) amplitude spectrum of the discrete-time LoRa waveforms. Our result shows that the DFT

energy spectrum of LoRa signals is constant and is the same for all LoRa waveforms.

LoRa also employs forward error correction (FEC) using binary block codes with code rate (CR) R_c equal to 4/5, 4/6, 4/7, or 4/8 [2]. For instance, when $R_c = 4/7$, three parity bits are appended to a message word with four bits to produce a codeword with seven bits. In the literature, the performance of the coded LoRa signals has been investigated in [25, 26]. In [25], Elshabrawy and Robert proposed a nonbinary code to further enhance the (binary) channel codes already considered in the LoRa literature [2, 12]. In [26], Afisiadis *et al.* investigated the frame error rate of coded LoRa using the error probability approximation proposed in [20] for uncoded LoRa.

In addition to the study of uncoded LoRa systems, this paper also extends our preliminary investigation done in [27] for coded LoRa systems. Specifically, this paper analyzes the probability of error for coded orthogonal LoRa signals in AWGN, assuming hard-decision decoding of the Hamming code defined in the LoRa physical layer. The resulting BER expressions are valid for both coherent and noncoherent cases and, differently from [27], are computed using the accurate approximations derived in this paper for uncoded LoRa. Simulation results validate the proposed analytical expressions and include the BER for a soft-decision channel decoder. With respect to [27], this paper proposes a simplified computation of the metrics used for soft-decision decoding, thereby reducing the decoder complexity from $O(M^2)$ to $O(M)$. We also consider multipath channels, by exploiting the channel model used in [14]. Both analytical and simulated results explain that the Hamming code of LoRa yields a significant performance gain with respect to uncoded LoRa, provided that the coded LoRa system uses lower bit rate and the same bandwidth of the LoRa uncoded system.

2. Uncoded LoRa

2.1. System Model

According to the patented LoRa physical layer in [12], the instantaneous frequency of the BB analog waveform grows linearly within a frequency range with bandwidth B, during the symbol period T_s, starting from an initial offset frequency and wrapping around the band limits, as expressed by

$$f_m(t) = \begin{cases} Kt + \xi_m, & t \in [0, \tau_m) \\ Kt + \xi_m - B, & t \in [\tau_m, T_s), \end{cases} \quad (1)$$

where $K = B/T_s$ is the analog frequency change rate, $T_s = M/B$ is the duration of the waveform, $\xi_m = mB/M$ is the initial frequency offset of the m-th chirp waveform ($m = 0, 1, \ldots, M-1$), and $\tau_m = (B - \xi_m)/K$. In (1), without loss of generality, we have assumed a bandwidth from 0 to B.

The m-th analog instantaneous phase is obtained as [28]

$$\begin{aligned} \phi_m(t) &= 2\pi \int_0^t f_m(t') \, dt' \\ &= \begin{cases} \pi Kt^2 + 2\pi\xi_m t, & t \in [0, \tau_m) \\ \pi Kt^2 - 2\pi(B - \xi_m)(t - T_s), & t \in [\tau_m, T_s), \end{cases} \end{aligned} \quad (2)$$

and the m-th analog BB waveform is

$$s_m(t) = e^{j\phi_m(t)}. \tag{3}$$

Note that (2) and (3) are in perfect agreement with the results of [15]. Upon sampling (3) at $f_s = B$, the m-th LoRa discrete-time waveform is expressed by

$$s_m[n] = e^{j\frac{\pi}{M}(n^2+2mn)}, \quad n \in \{0, \dots, M-1\}. \tag{4}$$

As shown in [15], differently from the LoRa analog waveforms (3), the LoRa discrete-time waveforms (4) are exactly orthogonal, since

$$\sum_{n=0}^{M-1} s_p[n] s_q^*[n] = \sum_{n=0}^{M-1} e^{j\frac{2\pi}{M}(p-q)n} = M\delta[p-q], \tag{5}$$

where $\delta[\cdot]$ is the Kronecker delta function. Since the correlation properties of the LoRa analog waveforms are different from those of the LoRa discrete-time waveforms, the performance of the LoRa analog model could be different from that of the LoRa discrete-time model. However, since in LoRa M is large enough ($M \geq 64$), the LoRa analog waveforms (3) are quasi-orthogonal [15], so we expect similar performance in both cases.

The DFT amplitude spectrum $S_m[k]$, defined as the M-point DFT of $s_m[n]$, is obtained as

$$S_m[k] = \sum_{n=0}^{M-1} e^{j\frac{\pi}{M}(n^2+2mn)} e^{-j\frac{2\pi}{M}nk} = G_M e^{-j\frac{\pi}{M}(m-k)^2}, \tag{6}$$

for $k, m \in \{0, \dots, M-1\}$, where $G_M = \sum_{n=0}^{M-1} e^{j\frac{\pi}{M}n^2} = \sqrt{\frac{M}{2}}(1+j)$ is a quadratic Gauss sum valid for M even [29, 30]. Consequently, the energy spectrum of all waveforms is constant in k and independent from m, as expressed by

$$|S_m[k]|^2 = |G_M|^2 = M, \quad k, m \in \{0, \dots, M-1\}. \tag{7}$$

This result explains that all the M LoRa discrete-time waveforms share the same portions of the spectrum: each waveform completely overlaps in frequency with the other $M-1$ waveforms. To the best of our knowledge, this constant feature of the DFT spectrum has not been previously highlighted. Figure 1 shows an example of the obtained discrete waveform and discrete energy spectrum, respectively, calculated for the waveform $s_m[n]$ with $m = 11$ and $M = 7$.

2.2. Symbol Detection

For simplicity, in the following we adopt a detector that is maximum likelihood (ML) when the waveforms are orthogonal. By denoting with $s_m[n]$ the transmitted waveform, if we consider an AWGN $w[n]$ with variance $\sigma_w^2 = N_0$, the received signal is expressed by $r[n] = s_m[n] + w[n]$. The ML detector uses a bank of M correlators that first perform a partial correla-
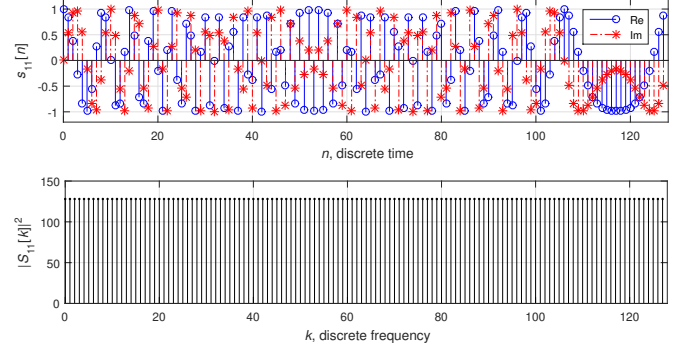

Figure 1: Discrete waveform and energy spectrum of a LoRa signal ($M = 7$).

tion expressed by

$$v_k[n] = r[n]s_k^*[n]$$
$$= (s_m[n] + w[n]) s_k^*[n], \quad k \in \{0, \dots, M-1\}, \tag{8}$$

and then perform the accumulation expressed by

$$\tilde{v}_k = \sum_{n=0}^{M-1} v_k[n]$$
$$= M\delta[k-m] + \tilde{w}_k, \quad k \in \{0, \dots, M-1\}, \tag{9}$$

where $\tilde{w}_k = \sum_{n=0}^{M-1} w[n] s_k^*[n]$ is a zero-mean complex Gaussian noise with variance $\sigma_{\tilde{w}}^2 = M\sigma_w^2$. Equivalently, the bank of M correlators in (8)–(9) can be replaced by a low-complexity single DFT operation applied to a downchirp partial correlator only [14], as expressed by

$$V[k] = \text{DFT}_M \{v_0[n]\}$$
$$= M\delta[k-m] + W'[k], \quad k \in \{0, \dots, M-1\}, \tag{10}$$

where $W'[k] = \sum_{n=0}^{M-1} w[n] s_0^*[n] e^{-j\frac{2\pi}{M}nk}$ is a zero-mean complex Gaussian noise with variance $\sigma_{W'}^2 = \sigma_{\tilde{w}}^2 = M\sigma_w^2$, and DFT_M stands for the DFT of size M. The coherent ML detector maximizes either $\text{Re}\{\tilde{v}_k\}$ in (9) or $\text{Re}\{V[k]\}$ in (10), while the noncoherent ML detector maximizes either $|\tilde{v}_k|$ in (9) or $|V[k]|$ in (10) [14, 20]. The phase coherence can be recovered by exploiting the training symbols inserted as a preamble in every LoRa packet [2, 13].

2.3. Existing BER Expressions

For LoRa with orthogonal waveforms in AWGN, the exact expression of the symbol error probability is given by Eq. 5-2-21 in [22, p. 262] and Eq. 5-4-46 in [22, p. 311]: Therefore, by considering $\kappa = M/(2(M-1))$ erroneous bits for each erroneous symbol, the exact BER for coherent and noncoherent detection, respectively, is

$$P_{b_C} = \frac{\kappa}{\sqrt{2\pi}} \int_{-\infty}^{+\infty} \left[1 - (1 - Q(y))^{M-1}\right] e^{-\frac{(y-\sqrt{2S\gamma_b})^2}{2}} \, dy, \tag{11}$$

$$P_{b_{NC}} = \kappa \sum_{l=1}^{M-1} (-1)^{l+1} \binom{M-1}{l} \frac{1}{l+1} e^{-\frac{l}{l+1}S\gamma_b}, \tag{12}$$

3

where $\gamma_b = E_b/N_0$ is the ratio between the energy per bit and the noise power spectral density, $Q(y)$ is the Gaussian tail function, S is the SF, and $M = 2^S$. As detailed in [27], the computation of the exact BER requires either a numerical evaluation of the integral (11) (in the case of coherent detection) or the computation of large binomial coefficients in (12) (in the case of noncoherent detection). Therefore, in both cases, the evaluation of the exact BER is computationally intensive. In addition, in the noncoherent case, usual arithmetic with 64-bit or 128-bit precision leads to incorrect results [27]. Consequently, simple BER approximations are required, as done in [20] for noncoherent detection of orthogonal LoRa, in [21] for coherent detection of quaternary modulations, and in [18] for coherent detection of quasi-orthogonal LoRa. Specifically, Elshabrawy and Robert (ER) proposed, for noncoherent orthogonal LoRa, the BER [20, Eq. 21]

$$P_{b_{\text{NC,ER}}} \approx 0.5 \, Q\left(\frac{\sqrt{M\Gamma} - (H_{M-1}^2 - \frac{\pi^2}{12})^{1/4}}{\sqrt{H_{M-1} - (H_{M-1}^2 - \frac{\pi^2}{12})^{1/2} + \frac{1}{2}}} \right), \quad (13)$$

where $\Gamma = \gamma_b S/M$ is the signal-to-noise ratio (SNR), $H_M = \sum_{m=1}^{M} \frac{1}{m}$ is the harmonic number of $M = 2^S$. In addition, Reynders and Pollin (RP) proposed another BER expression, valid for coherent detection of quasi-orthogonal LoRa, expressed by [18, Eq. 21]

$$P_{b_{\text{C,RP}}} = 0.5 \, Q\left(1.28 \sqrt{S\gamma_b} - 1.28 \sqrt{S} + 0.4 \right). \quad (14)$$

Both ER and RP expressions (13) and (14) are easier to calculate than (12) and (11), but the difference with (12) and (11) is not negligible. Therefore, other researchers have tried to increase accuracy at expense of complexity. For instance, [23] has proposed an improved approximation that makes use of the Marcum Q function, which is a two-dimensional function. In this paper, we aim at good BER approximations that use simpler one-dimensional functions, such as the Gaussian Q function used in [18, 20].

2.4. Proposed BER Approximations

We aim at simple approximations of (11)–(12), but with improved accuracy with respect to (13)–(14). Hence, we propose the following BER expressions for orthogonal LoRa. For coherent detection, we propose a BER approximation expressed by

$$P_{b_{\text{C,AP}}}(\gamma_b) = f_3(\gamma_b; \mathbf{p}_{\text{C}}) \, P_{b_{\text{C,UB}}}(\gamma_b), \quad (15)$$

where

$$P_{b_{\text{C,UB}}}(\gamma_b) = \frac{M}{2} \, Q\left(\sqrt{S\gamma_b} \right) \quad (16)$$

is the union bound (UB) on the bit error probability, and $f_3(\gamma_b; \mathbf{p}_{\text{C}})$ is a convenient function of γ_b representing the correction factor of the UB. The expression of this correction function $f_3(\gamma_b; \mathbf{p}_{\text{C}})$ will be explained later on in this section, as well as how to select the coefficients summarized by the vector $\mathbf{p}_{\text{C}}$. For noncoherent detection, similarly to (15) we propose a BER

approximation expressed by

$$P_{b_{\text{NC,AP}}}(\gamma_b) = f_3(\gamma_b; \mathbf{p}_{\text{NC}}) \, P_{b_{\text{NC,UB}}}(\gamma_b), \quad (17)$$

where

$$P_{b_{\text{NC,UB}}}(\gamma_b) = \frac{M}{4} e^{-S\frac{\gamma_b}{2}} \quad (18)$$

is the UB on the bit error probability for noncoherent detection, and $f_3(\gamma_b; \mathbf{p}_{\text{NC}})$ is the same correction function used for coherent detection, but with a different set of coefficients $\mathbf{p}_{\text{NC}}$. For simplicity, in the following we omit from $\mathbf{p}_{\text{C}}$ and $\mathbf{p}_{\text{NC}}$ the subscript denoting the coherent and noncoherent cases. Now, we explain how to select the correction function $f_3(\gamma_b; \mathbf{p})$ and its coefficients in the two cases. Specifically, we choose a function $f_3(\gamma_b; \mathbf{p})$ with two desired properties. First, for large γ_b, the term $f_3(\gamma_b; \mathbf{p})$ must tend to one, since at large SNR both the UBs (16) and (18) already tend to the correct BERs for coherent and noncoherent detectors, respectively: in other words, in the large SNR case, the correction factor must be ineffective, since the UB already gives a good approximation of the BER. Second, for low γ_b, the term $f_3(\gamma_b; \mathbf{p})$ must tend to $2/M$, because both the UBs (16) and (18) tend to $M/4$ when the SNR approaches zero, while the correct BER tend to $1/2$ for vanishing SNR: in other words, in the zero SNR case, a correction factor $2/M$ is necessary in order to attenuate the UB result $M/4$ to make it equal to the BER value $1/2$. Concerning the shape of the correction function $f_3(\gamma_b; \mathbf{p})$, we choose a rational function with cubic polynomials of γ_b at both numerator and denominator, as expressed by

$$f_3(\gamma_b; \mathbf{p}) = \frac{\gamma_b^3 + p_1\gamma_b^2 + p_2\gamma_b + p_3}{\gamma_b^3 + p_4\gamma_b^2 + p_5\gamma_b + \frac{M}{2}p_3}, \quad (19)$$

with $\mathbf{p} = [p_1 \, p_2 \, p_3 \, p_4 \, p_5]^T$ real coefficients to be optimized. The reason why we choose (19) is that the rational form leads to a simple computation of its coefficients. The use of cubic polynomials in (19) will produce the desired level of accuracy without using too many coefficients, as it will be shown in the next section. Note that, in (19), $\lim_{\gamma_b \to \infty} f_3(\gamma_b; \mathbf{p}) = 1$ and $f_3(0; \mathbf{p}) = 2/M$, as desired.

S	p_1	p_2	p_3	p_4	p_5
6	1.2272	1.0755	0.0914	0.2096	5.9406
7	1.0117	0.9216	0.0745	-0.0054	5.0523
8	0.9527	0.7446	0.0554	-0.0317	3.9555
9	1.1146	0.6089	0.0443	0.2706	2.0743
10	0.9699	0.3560	0.0260	0.2615	0.6248
11	0.6136	0.1782	0.0130	-0.0104	-0.0547
12	0.2817	0.0981	0.0064	-0.2683	-0.5299

Table 1: Values of $\mathbf{p} = \mathbf{p}_{\text{C}}$ in (19) for (15), coherent case.

To find $\mathbf{p}$, we use least-squares (LS) fitting. First, for the i-th value $\gamma_b^{(i)}$, we calculate $P_b^{(i)}$ using (11) or (12); to avoid the numerical instabilities of (11)–(12), we use high-precision GNU C libraries, such as GSL QAGI [31] for coherent detection and MPFR [32] for noncoherent detection. Second, we calculate the UB $P_{b_{\text{UB}}}^{(i)}$, yielding $f_3^{(i)} = P_b^{(i)}/P_{b_{\text{UB}}}^{(i)}$. Third, (15)–(17) can

S	p_1	p_2	p_3	p_4	p_5
6	1.6251	1.1170	0.2860	-0.3847	11.5459
7	1.2154	0.7663	0.1911	-0.6522	9.0367
8	0.8054	0.4780	0.1078	-0.8892	6.9659
9	0.4768	0.3070	0.0609	-1.0014	4.9693
10	0.2111	0.2095	0.0347	-0.9988	2.8935
11	-0.0076	0.1574	0.0199	-0.8901	0.6420
12	-0.1908	0.1336	0.0114	-0.6800	-1.8525

Table 2: Values of $\mathbf{p} = \mathbf{p}_{NC}$ in (19) for (17), noncoherent case.
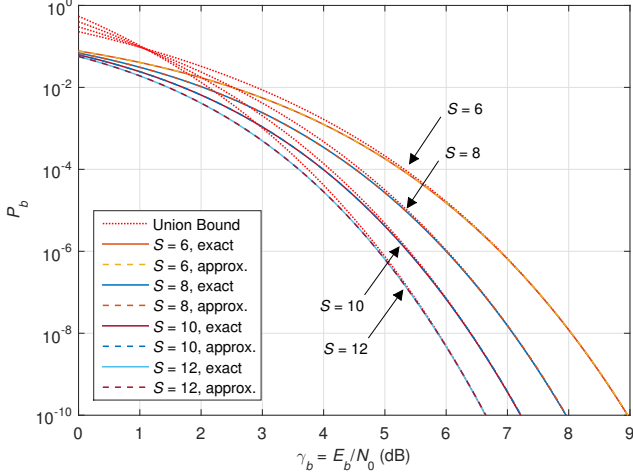
Figure 2: UB, exact, and approximated uncoded BER for coherent detection.

be rewritten as $u_i = \mathbf{q}_i^T \mathbf{p}$, where $u_i = (f_3^{(i)} - 1)(\gamma_b^{(i)})^3$ and $\mathbf{q}_i = [(\gamma_b^{(i)})^2, \gamma_b^{(i)}, 1 - Mf_3^{(i)}/2, -f_3^{(i)}(\gamma_b^{(i)})^2, -f_3^{(i)}\gamma_b^{(i)}]^T$. By using $F > 5$ values of $\gamma_b^{(i)}$, we obtain $\mathbf{u} = \mathbf{Q}\mathbf{p}$, where $\mathbf{u} = [u_1, u_2, \dots, u_F]^T$ and $\mathbf{Q} = [\mathbf{q}_1, \mathbf{q}_2, \dots, \mathbf{q}_F]^T$. The LS coefficients are then given by $\mathbf{p} = (\mathbf{Q}^T\mathbf{Q})^{-1} \mathbf{Q}^T \mathbf{u}$. Tables 1 and 2 report the coefficients $\mathbf{p} = \mathbf{p}_C$ and $\mathbf{p} = \mathbf{p}_{NC}$ (for coherent and noncoherent cases) for the spreading factors S used by LoRa. These coefficients produce, in both the numerator and the denominator of (19), cubic functions whose zeros are either real negative or complex. Therefore, both the numerator and the denominator of (19) are never zero, and hence (19) is meaningful in the whole range of SNR.

2.5. BER Comparison

Figures 2 and 3 compare the proposed BER (15)–(17) with the exact BER (11)–(12), for the coherent case and the noncoherent case, respectively, as a function of γ_b for different values of S. The exact BER (11)–(12) has been evaluated using high-complexity high-precision GNU C libraries (GSL QAGI [31] for coherent detection and MPFR [32] for noncoherent detection) to avoid numerical problems. In Figs. 2 and 3, we observe that the proposed BER approximation coincides with the exact BER, for all values of γ_b and S, and for both coherent and noncoherent cases. Figures 2 and 3 also show the corresponding UBs, which overestimate the BER: Therefore, the proposed correction function $f_3(\gamma_b; \mathbf{p})$ is effective and accurately counterbalances the BER overestimation of the UB at low SNR.
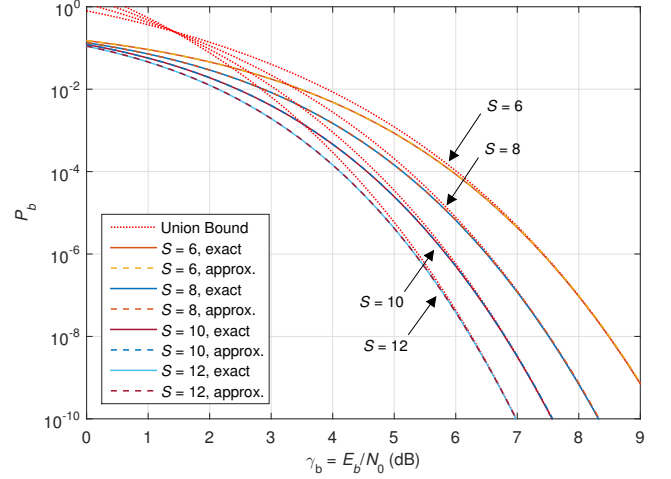

Figure 3: UB, exact, and approximated uncoded BER for noncoherent detection.
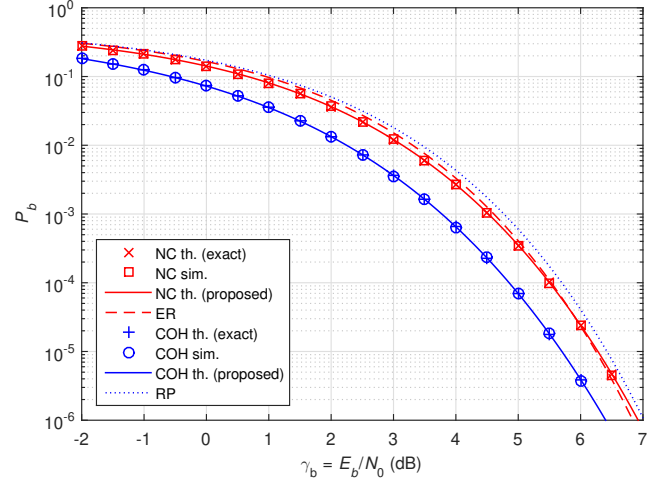

Figure 4: Uncoded BER for coherent and noncoherent detection ($S = 7$).

Figures 4–5 compare the simulated BER with the exact BER (11)–(12) and with the proposed BER (15)–(17). In the legends, we use the acronyms COH and NC to denote coherent and noncoherent detection, respectively. Figures 4–5 show that the simulated BER coincides with the theoretical BER (both exact and proposed expressions). For a BER of 10^{-6}, the SNR advantage of coherent detection, with respect to the noncoherent case, is about 0.53 dB for $S = 6$ and reduces with increasing S, up to 0.44 dB for $S = 12$. Figures 4–5 also compare the proposed BER with the existing BER expressions that use the Gaussian Q function. For noncoherent detection, the proposed BER is more accurate than the ER expression (13) of [20]. Figures 4–5 also show that the RP expression (14), used for nonorthogonal waveforms in [18], gives larger results than the BER of orthogonal LoRa. This agrees with the results of Fig. 3 of [18], which shows the difference between the RP expression and orthogonal FSK (whose performance is identical to the proposed expression).

Figure 6 presents the BER comparison as a function of the SF S, when $\gamma_b = 4$ dB. For all the SF values, the proposed BER
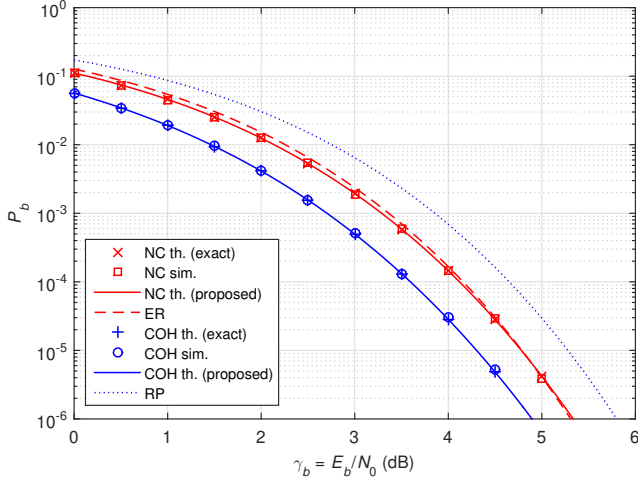
Figure 5: Uncoded BER for coherent and noncoherent detection ($S = 12$).

Figure 7: Uncoded BER of orthogonal and quasi-orthogonal waveforms.

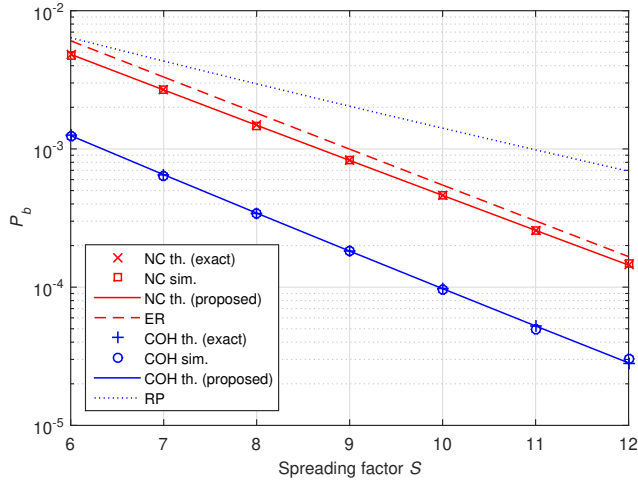

Figure 6: Uncoded BER for coherent and noncoherent detection ($E_b/N_0 = 4$ dB).

(15)–(17) coincides with the exact BER (11)–(12) and with the simulated results: This confirms that the proposed BER expressions are more accurate than the BER expressions ER (13) and RP (14) proposed in [20] and [18], respectively.

Figure 7 investigates the performance differences caused by using quasi-orthogonal analog LoRa waveforms instead of orthogonal discrete-time LoRa waveforms, for fixed $\gamma_b = E_b/N_0$. Figure 7 explains that, for the spreading factors of LoRa ($S \geq 6$), the BER performance is practically identical in the two cases. Some differences are present only if we would use spreading factors lower than those allowed in LoRa. These BER differences are low and reduce with increasing S: this is due to the waveform crosscorrelation coefficients, which are low and reduce with increasing S, as detailed in [15].

2.6. Complexity Comparison

Herein we verify that our proposed BER approximations are easier to compute than the exact BER expressions. To this purpose, we have computed the mean evaluation time of a single point of the BER curve, in the coherent and noncoherent cases,
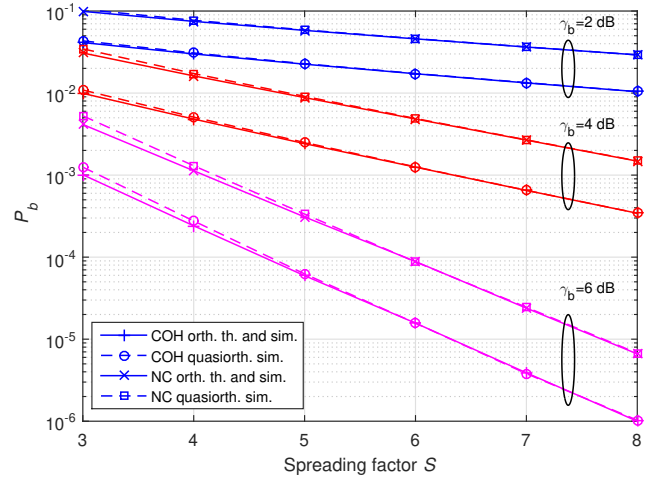
for both exact and approximated expressions. The BER evaluation programs are written in C language and have been compiled with GCC compiler version 9.3.0, using the GSL QAGI version 2.5 [31] and MPFR version 4.0.2 [32] libraries. The programs have been executed in a PC with Ubuntu OS and Core i7 860 CPU at 2.8 GHz. The results have been averaged over all γ_b points ranging from 0 dB to 9 dB, in steps of 0.1 dB.

In the case of coherent detection, the mean evaluation time of the exact BER expression (11) is 740 μs for $S = 6$ and then increases with S up to 2280 μs for $S = 12$. On the contrary, the mean evaluation time of our approximated BER expression (15) is 0.4 μs for all values of S: Therefore, in the coherent case, the computation of our BER approximation is more than one thousand times faster than the exact BER expression.

In the case of noncoherent detection, the correct evaluation of the exact expression (12) for $S = \log_2 M$ requires floating point arithmetic with M-bit precision [27], due to the computation of large binomial coefficients. Therefore, in the case of noncoherent detection, the mean evaluation time of the exact BER expression (12) is 440 μs for $S = 6$ and then increases with S up to 5.5 s for $S = 12$. On the contrary, the mean evaluation time of our approximated BER expression (17) is 0.1 μs for all values of S: Therefore, in the noncoherent case, the computation of our BER approximation is more than four thousand times faster than the exact BER expression.

3. Coded LoRa

3.1. System Model

Herein we adopt the matrix model [27] for the coded LoRa system represented in Fig. 8. We assume a Hamming block code with $k = 4$ information bits and $n = 7$ coded bits (CR is $R_c = 4/7$). We collect kS information bits into a vector, expressed by $\mathbf{b} = [b_0, \ldots, b_{kS-1}]^T$. This vector is reshaped as a $k \times S$ matrix, expressed by $\mathbf{B} = \text{unvec}_{k,S}(\mathbf{b})$, where $\text{unvec}_{k,S}(\cdot)$ represents the operator that writes the output elements column by column. Alternatively, the $k \times S$ matrix $\mathbf{B}$ can be expressed
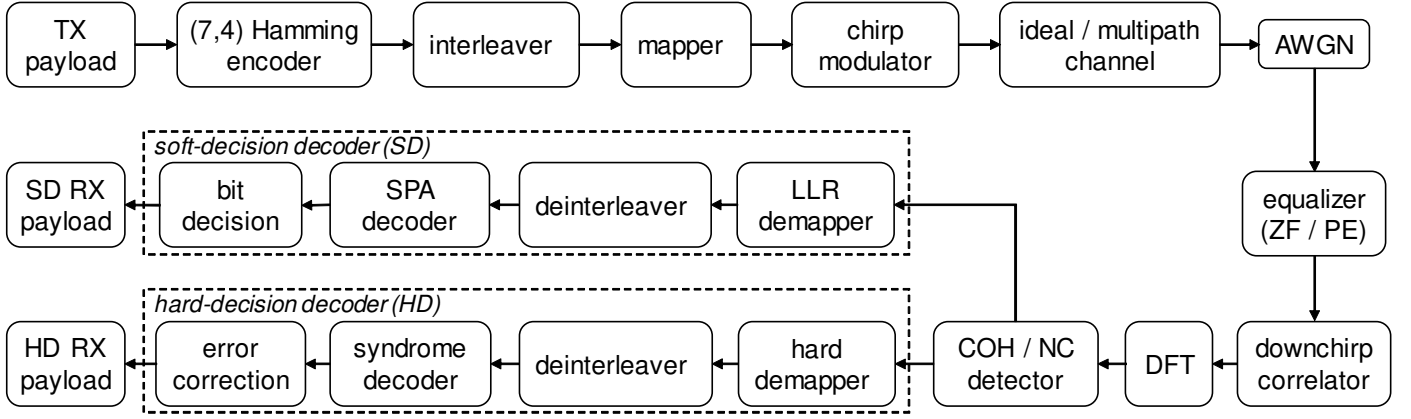
Figure 8: Block diagram of the coded LoRa system.

by

$$\mathbf{B} = [\mathbf{T}_0\mathbf{b}, \mathbf{T}_1\mathbf{b}, \ldots, \mathbf{T}_{S-1}\mathbf{b}], \tag{20}$$

where $\mathbf{T}_i$ is a $k \times kS$ matrix defined by

$$\mathbf{T}_i = [\mathbf{0}_{k \times ik}, \mathbf{I}_k, \mathbf{0}_{k \times (S-1-i)k}], \tag{21}$$

with $\mathbf{0}_{m \times n}$ the $m \times n$ zero matrix.

The S columns of $\mathbf{B}$ can be interpreted as S different k-bits messages, to be encoded into S n-bits codewords. The coded bits are obtained by

$$\mathbf{C} = (\mathbf{G}^T\mathbf{B})_2, \tag{22}$$

where $\mathbf{C}$, with dimensions $n \times S$, contains the S codewords column-wise, $\mathbf{G}$ is the $k \times n$ code generator matrix, and $(\cdot)_2$ stands for the element-wise modulo-2 operation. In a systematic $(7, 4)$ Hamming code, the generator matrix is $\mathbf{G} = [\mathbf{I}_4, \mathbf{P}]$, where the parity matrix $\mathbf{P}$ is expressed by

$$\mathbf{P} = \begin{bmatrix} 1 & 0 & 1 \\ 1 & 1 & 1 \\ 1 & 1 & 0 \\ 0 & 1 & 1 \end{bmatrix}. \tag{23}$$

The interleaver takes the S codewords in the columns of $\mathbf{C}$ and produces n binary vectors of S bits represented by rows of $\mathbf{C}$. Using binary-to-decimal conversion, these n vectors are transformed into n numbers, as expressed by

$$\mathbf{m} = [m_0, \ldots, m_{n-1}]^T = \mathbf{C}\mathbf{d}, \tag{24}$$

where $\mathbf{d} = [2^{S-1}, 2^{S-2}, \ldots, 4, 2, 1]^T$. Note that the S columns of $\mathbf{C}$ contain S different codewords. Therefore, each index m_i in (24) is obtained from S bits that belong to S different codewords, similarly to [12]. To be precise, in the LoRa document [12], the codewords are stored diagonally, while in the matrix $\mathbf{C}$ in (24) the codewords are stored by columns. However, each index m_i is obtained from S different codewords in both interleaving cases, and therefore the interleaver used in this paper produces the same bit error probability of the interleaver used in [12].

The decimal values in $\mathbf{m}$ in (24) are the n indexes of the LoRa symbols (waveforms) to be transmitted in n consecutive time intervals. We define $\mathbf{s}_m$ as the vector containing the M samples of the m-th LoRa waveform expressed by (4). The n LoRa waveforms, consecutively transmitted, are inserted into an $M \times n$ matrix $\mathbf{S} = [\mathbf{s}_{m_0}, \ldots, \mathbf{s}_{m_{n-1}}]$, which is reshaped as a vector $\mathbf{s} = \text{vec}(\mathbf{S})$ with size Mn, where $\text{vec}(\cdot)$ is the vectorization operator that stacks the columns of a matrix into a single vector. This vector $\mathbf{s}$ is transmitted through a wireless multipath channel with finite impulse response (FIR) $\mathbf{a} = [a_0, \ldots, a_L]$ of order L. By defining the $(Mn + L) \times Mn$ channel matrix $\mathbf{A} = \text{Toeplitz}(\mathbf{a})$, the received vector $\mathbf{r}$ after the multipath channel is expressed by

$$\mathbf{r} = \mathbf{A}\mathbf{s} + \mathbf{w}, \tag{25}$$

where the AWGN is represented by $\mathbf{w}$, whose size is $Mn + L$.

3.2. Equalization and Detection

For simplicity, we assume perfect synchronization and perfect channel state information at the receiver. By using an $Mn \times (Mn + L)$ linear equalization matrix $\mathbf{L}$, the received vector in (25) is transformed into the equalized vector $\mathbf{r}_{\text{eq}}$ expressed by

$$\mathbf{r}_{\text{eq}} = \mathbf{L}\mathbf{r} = \mathbf{s} + \mathbf{z}, \tag{26}$$

where $\mathbf{z} = \mathbf{L}\mathbf{A}\mathbf{s} - \mathbf{s} + \mathbf{L}\mathbf{w}$ is the intersymbol interference (ISI) plus noise at the output of the equalizer. The equalizer $\mathbf{L}$ can be designed according to different criteria, such as zero-forcing (ZF) equalization, as expressed by

$$\mathbf{L}_{\text{ZF}} = (\mathbf{A}^H\mathbf{A})^{-1}\mathbf{A}^H, \tag{27}$$

or phase equalization (PE) of the first channel path (which is assumed to be the strongest path), as expressed by

$$\mathbf{L}_{\text{PE}} = \frac{a_0^*}{|a_0|}[\mathbf{I}_{Mn}, \mathbf{0}_{Mn \times 1}], \tag{28}$$

or by other linear equalizers. The elements of $\mathbf{r}_{\text{eq}}$ are reshaped into the $M \times n$ matrix $\mathbf{R}_{\text{eq}} = \text{unvec}_{M,n}(\mathbf{r}_{\text{eq}})$, which gives

$$\mathbf{R}_{\text{eq}} = \mathbf{S} + \mathbf{Z}, \tag{29}$$

where $\mathbf{Z} = \text{unvec}_{M,n}(\mathbf{z})$ collects residual ISI and noise.

The detector performs first an element-wise multiplication between the equalized vector (i.e., a column of $\mathbf{R}_{\text{eq}}$) and the downchirp vector $\mathbf{s}_0^*$. Successively, the detector takes DFT of the obtained product [14]. This is repeated for all the n symbols (columns) in $\mathbf{R}_{\text{eq}}$. We define the multiple-downchirp matrix $\mathbf{S}_0 = \mathbf{1}_{1 \times n} \otimes \mathbf{s}_0^*$, where $\otimes$ is the Kronecker product, $\mathbf{1}_{1 \times n}$ is the row vector with n ones, and $(\cdot)^*$ denotes complex conjugation. By applying the multiple-downchirp matrix $\mathbf{S}_0$, $\mathbf{R}_{\text{eq}}$ in (29) becomes

$$\mathbf{U} = \mathbf{S}_0 \odot \mathbf{R}_{\text{eq}} = \mathbf{S}_0 \odot \mathbf{S} + \mathbf{Z}_{\mathbf{U}}, \tag{30}$$

where $\odot$ is the Hadamard product and $\mathbf{Z}_{\mathbf{U}} = \mathbf{S}_0 \odot \mathbf{Z}$ is the noise term. By defining $\mathbf{F}$ as the unitary DFT matrix of size M, we obtain

$$\mathbf{V} = \mathbf{F}\mathbf{U} = \mathbf{F}(\mathbf{S}_0 \odot \mathbf{S}) + \mathbf{Z}_{\mathbf{F}}, \tag{31}$$

where $\mathbf{Z}_{\mathbf{F}} = \mathbf{F}(\mathbf{S}_0 \odot \mathbf{Z})$ is the noise in the frequency domain. If we denote with v_{ij} the (i, j)-th element of $\mathbf{V}$ in (31), the non-coherent symbol estimate of the j-th LoRa waveform is given by

$$\hat{m}_j^{(\text{NC})} = \arg \max_i |v_{ij}|^2, \tag{32}$$

while the coherent symbol estimate is

$$\hat{m}_j^{(\text{COH})} = \arg \max_i \text{Re}\{v_{ij}\}. \tag{33}$$

Then we collect the n estimated symbol indexes (obtained either using (32) or (33) for $j = 0, \ldots, n-1$) into a single vector $\hat{\mathbf{m}} = [\hat{m}_0, \ldots, \hat{m}_{n-1}]^T$. By decimal-to-binary conversion, we obtain the $n \times S$ matrix $\hat{\mathbf{C}}$ expressed by

$$\hat{\mathbf{C}} = \left(\left\lfloor \left[\frac{\hat{\mathbf{m}}}{2^{S-1}}, \frac{\hat{\mathbf{m}}}{2^{S-2}}, \ldots, \frac{\hat{\mathbf{m}}}{4}, \frac{\hat{\mathbf{m}}}{2}, \hat{\mathbf{m}} \right] \right\rfloor \right)_2 \tag{34}$$

where $\lfloor \cdot \rfloor$ represents the element-wise integer part. The n rows of $\hat{\mathbf{C}}$ represent n LoRa symbols, of S bits each. By deinterleaving, $\hat{\mathbf{C}}$ is read column-wise, and hence we obtain S received codewords of n bits each, to be passed to the channel decoder.

3.3. Hard Decision Decoding

Hard decision decoding requires three steps: syndrome calculation, error pattern computation, and error correction. The syndrome matrix $\mathbf{Y}$, of dimensions $(n-k) \times S$, is obtained as

$$\mathbf{Y} = (\mathbf{H}\hat{\mathbf{C}})_2, \tag{35}$$

where $\mathbf{H} = [\mathbf{P}^T, \mathbf{I}_{n-k}]$ is the parity-check matrix. The error pattern is obtained by the coset leader of the standard array [22]. By denoting with $\mathbf{y}_i$ the i-th column of $\mathbf{Y}$, the error pattern $\hat{\mathbf{e}}_i$ is a column vector of size k obtained as $\hat{\mathbf{e}}_i = \text{coset}(\mathbf{y}_i)$, where $\text{coset}(\cdot)$ produces the first k bits of the coset leader corresponding to the syndrome $\mathbf{y}_i$. Specifically, for the (7, 4) Hamming code (23), $\text{coset}(\cdot)$ produces $\hat{\mathbf{e}}_i = [1, 0, 0, 0]^T$ when $\mathbf{y}_i = [1, 0, 1]^T$, $\hat{\mathbf{e}}_i = [0, 1, 0, 0]^T$ when $\mathbf{y}_i = [1, 1, 1]^T$, $\hat{\mathbf{e}}_i = [0, 0, 1, 0]^T$ when $\mathbf{y}_i = [1, 1, 0]^T$, $\hat{\mathbf{e}}_i = [0, 0, 0, 1]^T$ when $\mathbf{y}_i = [0, 1, 1]^T$, and $\hat{\mathbf{e}}_i = [0, 0, 0, 0]^T$ in the other four syndrome cases, i.e., when $\mathbf{y}_i$

has more zeros than ones. Hence, the $k \times S$ estimated error is obtained as $\hat{\mathbf{E}} = [\hat{\mathbf{e}}_0, \ldots, \hat{\mathbf{e}}_{S-1}]$, and the final bit estimate $\hat{\mathbf{B}}$ is obtained as

$$\hat{\mathbf{B}} = (\mathbf{J}\hat{\mathbf{C}} + \hat{\mathbf{E}})_2, \tag{36}$$

where $\mathbf{J} = [\mathbf{I}_k, \mathbf{0}_{k \times (n-k)}]$ is the matrix that removes the $(n - k)$ parity bits.

3.4. BER after Hard Decision Decoding

In this subsection, we assume an AWGN channel, that is, in (25)–(26), we assume $L = 0$, $a_0 = 1$, and $\mathbf{A} = \mathbf{I}_{Mn} = \mathbf{L}$, so that $\mathbf{z} = \mathbf{w}$ in (26). In this case, equalization is unnecessary. For orthogonal chirp waveforms, the BER p of the coded bits $\mathbf{C}$ can be approximated as in (15) and (17), for coherent and noncoherent detection, respectively. Since the Hamming code is a perfect code, the probability of bit error on the message bits $\mathbf{B}$ can be well approximated by (Eq. 8-1-82 in [22, p. 453])

$$P = \frac{2t + 1}{n} \sum_{j=t+1}^{n} \binom{n}{j} p^j (1 - p)^{n-j} \tag{37}$$

$$= \frac{2t + 1}{n} \left(1 - \sum_{j=0}^{t} \binom{n}{j} p^j (1 - p)^{n-j} \right), \tag{38}$$

where t is the number of correctable errors in each block. For the (7, 4) Hamming code, (37) becomes

$$P = \frac{3}{7} \sum_{j=2}^{7} \binom{7}{j} p^j (1 - p)^{7-j} \tag{39}$$

$$= 3p^2 \left(3 - 10p + 15p^2 - 12p^3 + 5p^4 - \frac{6}{7}p^5 \right). \tag{40}$$

For coherent detection, (39) is computed using our proposed expression (15), based on (19) with the values of Table 1. For noncoherent detection, (39) is computed using our proposed expression (17), where (19) uses the values of Table 2.

3.5. Soft Decision Decoding

The first step of soft decision decoding is the calculation of the log-likelihood ratios (LLR) of the codeword bits, while the second step is the message-passing decoding of the message bits using the sum-product algorithm (SPA). By denoting the decision variable with $v_{ij} = |v_{ij}|^2$ in (32) or $v_{ij} = \text{Re}\{v_{ij}\}$ in (33)), and assuming that the elements v_{ij} are independent Gaussian variables, the LLR $\mathcal{L}_{j\lambda}$ for the λ-th bit of $\hat{m}_j$ is obtained as [33]

$$\mathcal{L}_{j\lambda} = \log \frac{\sum_{m \in \mathcal{M}_1(\lambda)} \prod_{i=0}^{M-1} f_{v_{ij}|\mathbf{s}_m}(v_{ij})}{\sum_{m' \in \mathcal{M}_0(\lambda)} \prod_{i'=0}^{M-1} f_{v_{i'j}|\mathbf{s}_{m'}}(v_{i'j})}, \tag{41}$$

where $\mathcal{M}_1(\lambda)$ is the set of $M/2$ indexes such that the λ-th bit in the binary representation of m is 1, $\mathcal{M}_0(\lambda)$ is the set of $M/2$ indexes such that the λ-th bit in the binary representation of m is 0, and $f_{v_{ij}|\mathbf{s}_m}(v_{ij})$ is the conditional probability density function (pdf) of v_{ij} given that the signal $\mathbf{s}_m$ has been transmitted. For the coherent case, we approximate the conditional pdfs at the

numerator and at the denominator of (41) by assuming $\mathbf{z} \approx \mathbf{w}$ in (26), which gives, for $m \in \mathcal{M}_1(\lambda)$,

$$f_{\nu_{ij}|\mathbf{s}_m}^{(\text{COH})}(\nu_{ij}) = \frac{1}{\sqrt{2\pi}\sigma_z} e^{-\frac{(\nu_{ij}-M\delta[i-m])^2}{2\sigma_z^2}}, \tag{42}$$

where σ_z^2 is the variance of each element in $\text{Re}\{\mathbf{z}\} \approx \text{Re}\{\mathbf{w}\}$ in (26). By inserting (42) in (41), we obtain

$$\mathcal{L}_{j\lambda}^{(\text{COH})} = \log \frac{\sum\limits_{m \in \mathcal{M}_1(\lambda)} e^{\frac{M\nu_{mj}}{\sigma_z^2}}}{\sum\limits_{m' \in \mathcal{M}_0(\lambda)} e^{\frac{M\nu_{m'j}}{\sigma_z^2}}}. \tag{43}$$

Similarly, for the noncoherent detector, the conditional pdfs are given by

$$f_{\nu_{ij}|\mathbf{s}_m}^{(\text{NC})}(\nu_{ij}) = \frac{1}{2\sigma_z^2} e^{-\frac{\nu_{ij}+M^2\delta[i-m]}{2\sigma_z^2}} \text{I}_0\left(\frac{M\sqrt{\nu_{ij}}}{\sigma_z^2}\delta[i-m]\right), \tag{44}$$

where $\text{I}_0(\cdot)$ is the modified Bessel function of the first kind of order 0. By inserting (44) in (41), we obtain

$$\mathcal{L}_{j\lambda}^{(\text{NC})} = \log \frac{\sum\limits_{m \in \mathcal{M}_1(\lambda)} \text{I}_0\left(\frac{M\sqrt{\nu_{mj}}}{\sigma_z^2}\right)}{\sum\limits_{m' \in \mathcal{M}_0(\lambda)} \text{I}_0\left(\frac{M\sqrt{\nu_{m'j}}}{\sigma_z^2}\right)}. \tag{45}$$

By denoting with $\mathcal{L}_{j\lambda}^{(\iota)}$ the LLRs at the input of the SPA for the $(\iota + 1)$-th iteration, the iterative message-passing decoder based on the sum-product rule [34] produces the updated LLRs $\mathcal{L}_{j\lambda}^{(\iota+1)}$. The SPA initialization uses $\mathcal{L}_{j\lambda}^{(0)} = \mathcal{L}_{j\lambda}$. At every iteration step ι, the algorithm updates the LLR values using the *tanh* rule [34] on the Tanner graph of the (7, 4) Hamming code. The process stops after $\iota_{\max}$ iterations. At the end, the entries of the estimated message matrix $\tilde{\mathbf{B}}$ are obtained by hard-decision on the final LLR values as $\tilde{b}_{ij} = (\text{sign}(\mathcal{L}_{ji}^{(\iota_{\max})}) + 1)/2$, where $\text{sign}(\cdot)$ stands for the signum function.

Note that using the simplified LLR expressions (43) and (45), the complexity of the soft decoder is $O(M)$. Therefore, the decoding complexity is reduced by a factor M with respect to the decoder in [27] based on (41), whose complexity is $O(M^2)$.

3.6. Simulation Results

This section aims at validating the analytical BER expressed in (39) for coded LoRa in AWGN channels, in order to assess the SNR gain produced by hard-decision decoding (HD) of the (7, 4) Hamming code. In addition, this section investigates by simulation the SNR gain obtained using soft-decision decoding (SD), also in multipath channels. We assume that both uncoded and coded LoRa systems use the same SNR Γ and the same bandwidth, so the bit rate for the coded LoRa is $R_c = 4/7$ times lower than for the uncoded (UNC) LoRa. The SNR is defined as in [25] by $\Gamma = \gamma_b S/M$.

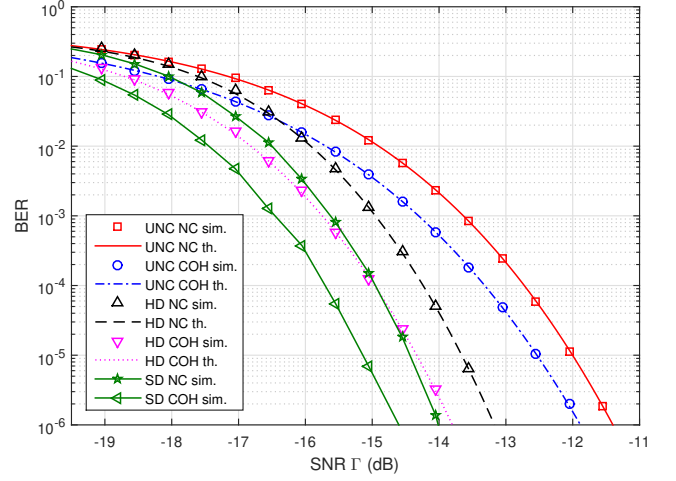Figures 9–10 compare the theoretical BER with the simulated BER, as a function of the SNR, when the SF is $S = 9$
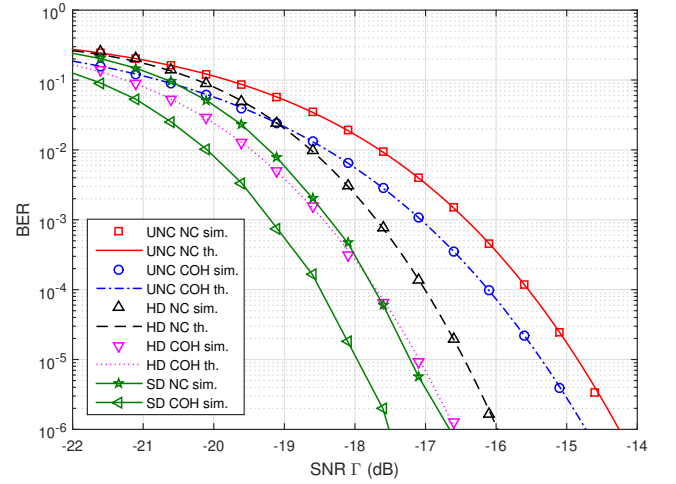

Figure 9: Coded BER in AWGN channel ($S = 9$).

Figure 10: Coded BER in AWGN channel ($S = 10$).

and $S = 10$, respectively. In these figures, the theoretical BER has been calculated using both the exact expression and the proposed approximated expression: since both curves coincide (like in the UNC case), to simplify the figure legend, only one curve is shown. Figures 9–10 show that theory and simulations are in agreement, also in coded LoRa, for both coherent (COH) and noncoherent (NC) detection. Fig. 9 explains that, for $S = 9$, the SNR gain of HD is 1.8 dB for COH detection and 1.7 dB for NC detection, when the BER is 10^{-5}. Using SD with $\iota_{\max} = 50$ iterations, the SNR gain (with respect to UNC transmission) increases to 2.6 dB for COH detection and to 2.4 dB for NC detection. Fig. 10 shows that, for $S = 10$ and BER equal to 10^{-5}, HD produces an SNR gain of 1.7 dB for COH detection and 1.6 dB for NC detection. In this case, using SD gives an additional gain of 0.9 dB for COH detection and 0.8 dB for NC detection with respect to HD.

Figs. 11–12 exhibit the BER in multipath channels, assuming the two-paths channel introduced in [14]. We consider two cases: $S = 9$ with COH detection in Fig. 11 and $S = 10$ with NC detection in Fig. 12. Two different linear equalizers are em-
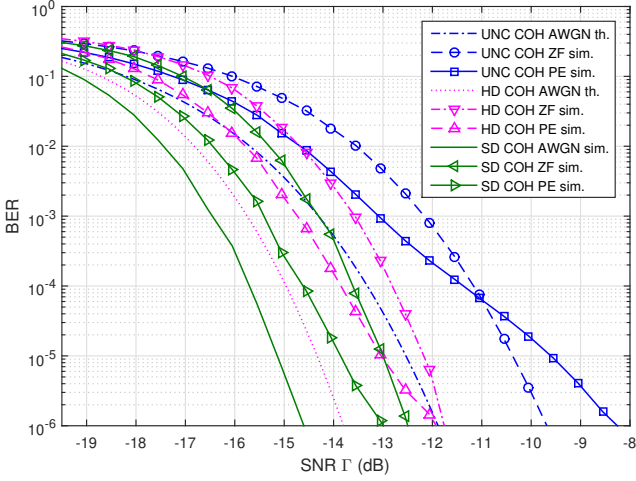
Figure 11: Coded BER in multipath channel ($S = 9$).

Figure 12: Coded BER in multipath channel ($S = 10$).

ployed: the ZF equalizer (27), and the PE equalizer (28). The ZF equalizer has been implemented as a three-taps FIR filter obtained by approximating the full ZF equalizer in (27). Note that the PE in (28) only compensates for the phase-shift of the largest path, which is assumed to be the first one. Fig. 11 shows the BER for $S = 9$ with COH detection. In this multipath channel, with respect to the AWGN case, for UNC transmission at BER of 10^{-5}, ZF outperforms PE. Differently, choosing a BER of 10^{-3}, PE improves upon ZF. Indeed, at low SNR the effect of the noise is more evident with respect to the residual ISI; therefore, at low SNR, PE outperforms ZF because the residual ISI at the output of the PE equalizer is reduced with respect to the noise amplified by the ZF. On the other hand, at large SNR, the residual interference of the PE is larger than the noise at the output of the ZF equalizer. In detail, for UNC transmission in AWGN, at BER of 10^{-5}, there is an SNR loss of 2.2 dB for ZF and 2.9 dB for PE. In the coded case, the situation at BER of 10^{-5} is similar to UNC transmission at BER of 10^{-3}, hence where the PE outperforms ZF. Specifically, for coded transmissions with HD, at BER of 10^{-5} there is a loss of 1.3 dB with PE and 2.2 dB with ZF, with respect to AWGN. Similarly, for coded transmissions with SD, there is a loss of 1.3 dB with PE and 2.1 dB with ZF. For both ZF and PE, the SNR gain of SD with respect to HD is between 0.8 dB and 0.9 dB.

Fig. 12 shows the BER for $S = 10$ with NC detection in multipath channels. Similarly to the COH detection case with $S = 9$, PE outperforms ZF at low SNR, and ZF outperforms PE at high SNR. The SNR value at which the PE and ZF achieve the same BER is different in the UNC, HD, and SD cases. At BER of 10^{-5}, there is an SNR loss of 2.2 dB with ZF and 3.6 dB with PE, in the UNC case. In the coded case with HD, instead, there is a loss of 2.1 dB with ZF and 2.2 dB with PE. Differently, in the coded case with SD, the loss is of 2.0 dB with PE and 2.1 dB with ZF. In both coded cases, the SNR loss is quite similar: indeed, in both cases, PE and ZF have approximately the same performance at BER equal to 10^{-5}. The SNR gain of SD with respect to HD is 0.7 dB for PE, and 1 dB for ZF.
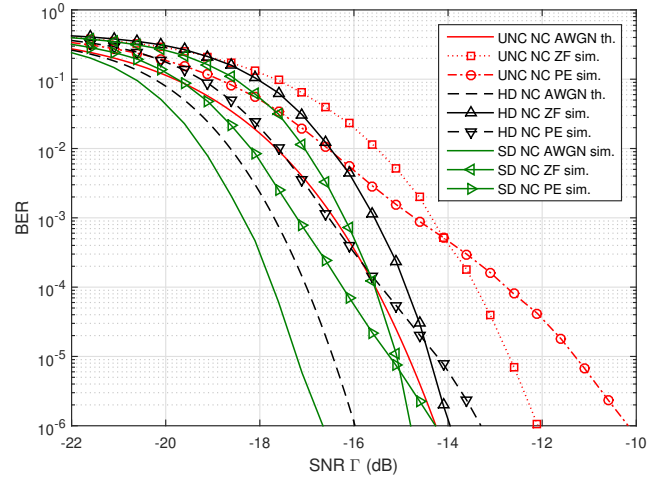
4. Conclusion

This paper has investigated the BER performance of LoRa systems using uncoded and coded transmission with coherent and noncoherent detection. We have proposed accurate BER approximations for uncoded LoRa signals with coherent (or noncoherent) detection, and for Hamming coded LoRa signals with hard channel decoding and coherent (or noncoherent detection), both in AWGN channels. The proposed approximations can be calculated with a complexity similar to other existing approximations but have improved accuracy. In this paper, we have also verified by means of simulations that quasi-orthogonal analog LoRa systems have the same performance of orthogonal discrete-time LoRa systems. The performance has been simulated also in multipath channel, by exploiting simplified equalizers at the receiver side. Finally, we have proposed a reduced-complexity method for soft decoding of coded LoRa signals: this method is suitable for low-power devices and provides an SNR advantage of up to 1 dB with respect to hard decoding.

Declaration of competing interest

The authors declare that they have no known competing financial interests or personal relationships that could have appeared to influence the work reported in this paper.

References

[1] U. Raza, P. Kulkarni, M. Sooriyabandara, Low power wide area networks: An overview, IEEE Commun. Surveys Tuts. 19 (2017) 855–873. doi:10.1109/COMST.2017.2652320.

[2] A. Augustin, J. Yi, T. Clausen, W. M. Townsley, A study of LoRa: Long range & low power networks for the Internet of Things, Sensors 16 (2016) doi:10.3390/s16091466.

[3] T. Xu, I. Darwazeh, Non-orthogonal narrowband Internet of Things: A design for saving bandwidth and doubling the number of connected devices, IEEE Internet Things J. 5 (2018) 2120–2129. doi:10.1109/JIOT.2018.2825098.

[4] L. Rugini, G. Baruffa, Performance of nonorthogonal FSK for the Internet of Things, Digital Signal Process. 85 (2019) 124–133. doi:10.1016/j.dsp.2018.11.011.

[5] O. M. Bushnaq, A. Chaaban, S. P. Chepuri, G. Leus, T. Y. Al-Naffouri, Sensor placement and resource allocation for energy harvesting IoT networks, Digital Signal Process. (In press).

[6] F. Adelantado, X. Vilajosana, P. Tuset-Peiro, B. Martinez, J. Melia-Segui, T. Watteyne, Understanding the limits of LoRaWAN, IEEE Commun. Mag. 55 (2017) 34–40. doi:10.1109/MCOM.2017.1600613.

[7] J. Petäjäjärvi, K. Mikhaylov, M. Hämäläinen, J. Iinatti, Evaluation of LoRa LPWAN technology for remote health and wellbeing monitoring, in: Proc. 10th Int. Symp. Medical Inform. Commun. Technol. (ISMICT), Worcester, MA, USA, 2016, pp. 1–5. doi:10.1109/ISMICT.2016.7498898.

[8] Q. Li, Z. Liu, J. Xiao, A data collection collar for vital signs of cows on the grassland based on LoRa, in: Proc. 15th Int. Conf. e-Business Eng. (ICEBE), Xi'an, China, 2018, pp. 213–217. doi:10.1109/ICEBE.2018.00041.

[9] L. Germani, V. Mecarelli, G. Baruffa, L. Rugini, F. Frescura, An IoT architecture for continuous livestock monitoring using LoRa LPWAN, Electronics 8 (2019) 1435. doi:10.3390/electronics8121435.

[10] J. Haxhibeqiri, A. Karaagac, F. Van den Abeele, W. Joseph, I. Moerman, J. Hoebeke, LoRa indoor coverage and performance in an industrial environment: Case study, in: Proc. 22nd IEEE Int. Conf. Emerging Technol. Factory Autom. (ETFA), Limassol, Cyprus, 2017, pp. 1–8. doi:10.1109/ETFA.2017.8247601.

[11] M. S. Sardar, Y. Yi, W. Xue-fen, J. Huang, J. Zhang, X. Qin, Q. Zhao, Y. Wang, M. A. Iqbal, Experimental analysis of LoRa CSS wireless transmission characteristics for forestry monitoring and sensing, in: Proc. Int. Symp. Sensing and Instrumentation in IoT Era (ISSI), Shanghai, China, 2018, pp. 01249–01254. doi:10.1109/ISSI.2018.8538171.

[12] O. Seller, N. Sornin, Low power long range transmitter, 2014. US Patent 9,252,834 and EU Patent EP 2 763 321 A1.

[13] LoRa^TM Modulation Basics, Technical Report AN1200.22, Semtech Corporation, 2015.

[14] L. Vangelista, Frequency shift chirp modulation: The LoRa modulation, IEEE Signal Process. Lett. 24 (2017) 1818–1821. doi:10.1109/LSP.2017.2762960.

[15] M. Chiani, A. Elzanaty, On the LoRa modulation for IoT: Waveform properties and spectral analysis, IEEE Internet of Things Journal 6 (2019) 8463–8470. doi:10.1109/JIOT.2019.2919151.

[16] T. Søndrol, B. Jalaian, N. Suri, Investigating LoRa for the Internet of battlefield things: A cyber perspective, in: Proc. IEEE Military Commun. Conf. (MILCOM), Los Angeles, CA, USA, 2018, pp. 749–756. doi:10.1109/MILCOM.2018.8599805.

[17] G. Ferré, A. Giremus, LoRa physical layer principle and performance analysis, in: Proc. 25th IEEE Int. Conf. on Electron., Circuits and Syst. (ICECS), Bordeaux, France, 2018, pp. 65–68. doi:10.1109/ICECS.2018.8617880.

[18] B. Reynders, S. Pollin, Chirp spread spectrum as a modulation technique for long range communication, in: Proc. Symp. Commun. Veh. Technol. (SCVT), Mons, Belgium, 2016, pp. 1–5. doi:10.1109/SCVT.2016.7797659.

[19] S. Verdú, Multiuser Detection, Cambridge University Press, Cambridge, 1998.

[20] T. Elshabrawy, J. Robert, Closed-form approximation of LoRa modulation BER performance, IEEE Commun. Lett. 22 (2018) 1778–1781. doi:10.1109/LCOMM.2018.2849718.

[21] L. Rugini, Tight upper bounds on the probability of error of quaternary simplex signals, IEEE Commun. Lett. 19 (2015) 1001–1004. doi:10.1109/LCOMM.2015.2424691.

[22] J. G. Proakis, Digital Communications (3rd ed.), McGraw-Hill, New York, 1995.

[23] J. Courjault, B. Vrigneau, M. Gautier, O. Berder, Accurate LoRa perfor-mance evaluation using Marcum function, in: 2019 IEEE Global Communications Conference (GLOBECOM), Waikoloa, HI, USA, 2019, pp. 1–5. doi:10.1109/GLOBECOM38437.2019.9014148.

[24] O. Afisiadis, M. Cotting, A. Burg, A. Balatsoukas-Stimming, On the error rate of the LoRa modulation with interference, IEEE Trans. Wireless Commun. 19 (2020) 1292–1304. doi:10.1109/TWC.2019.2952584.

[25] T. Elshabrawy, J. Robert, Enhancing LoRa capacity using non-binary single parity check codes, in: 2018 14th International Conference on Wireless and Mobile Computing, Networking and Communications (WiMob), Limassol, Cyprus, 2018, pp. 1–7. doi:10.1109/WiMOB.2018.8589188.

[26] O. Afisiadis, A. Burg, A. Balatsoukas-Stimming, Coded LoRa frame error rate analysis, 2019. arXiv:1911.10245.

[27] G. Baruffa, L. Rugini, V. Mecarelli, L. Germani, F. Frescura, Coded LoRa performance in wireless channels, in: 2019 IEEE 30th Annual International Symposium on Personal, Indoor and Mobile Radio Communications (PIMRC), 2019, pp. 1–6. doi:10.1109/PIMRC.2019.8904298.

[28] B. Boashash, Estimating and interpreting the instantaneous frequency of a signal, Part I, Fundamentals, Proc. of the IEEE 80 (1992) 520–538. doi:10.1109/5.135376.

[29] B. C. Berndt, R. J. Evans, The determination of Gauss sums, Bulletin of the American Mathematical Society 5 (1981) 107–129. doi:10.1090/S0273-0979-1981-14930-2.

[30] P. G. Casazza, M. Fickus, Fourier transforms of finite chirps, EURASIP Journal on Advances in Signal Processing 2006 (2006) 070204. doi:10.1155/ASP/2006/70204.

[31] M. Galassi et al., GNU Scientific Library Reference Manual (3rd ed.), 2016.

[32] L. Fousse, G. Hanrot, V. Lefèvre, P. Pélissier, P. Zimmermann, MPFR: A multiple-precision binary floating-point library with correct rounding, ACM Trans. Math. Softw. 33 (2007). doi:10.1145/1236463.1236468.

[33] M. K. Simon, R. Annavajjala, On the optimality of bit detection of certain digital modulations, IEEE Trans. Commun. 53 (2005) 299–307. doi:10.1109/TCOMM.2004.841959.

[34] J. Chen, A. Dholakia, E. Eleftheriou, M. P. C. Fossorier, X.-Y. Hu, Reduced-complexity decoding of LDPC codes, IEEE Trans. Commun. 53 (2005) 1288–1299. doi:10.1109/TCOMM.2005.852852.